

# Cryo-EM structures of PI3K $\alpha$ reveal conformational changes during inhibition and activation

Xiao Liu<sup>a,1,2</sup>, Su Yang<sup>b,1,2</sup>, Jonathan R. Hart<sup>b,2</sup>, Yingna Xu<sup>a</sup>, Xinyu Zou<sup>c</sup>, Huibing Zhang<sup>d,e</sup>, Qingtong Zhou<sup>f</sup>, Tian Xia<sup>c</sup>, Yan Zhang<sup>d,e</sup>, Dehua Yang<sup>g,h,i,3</sup>, Ming-Wei Wang<sup>a,f,g,h,i,j,3</sup>, and Peter K. Vogt<sup>b,3</sup>

<sup>a</sup>School of Pharmacy, Fudan University, Shanghai 201203, China; <sup>b</sup>Department of Molecular Medicine, The Scripps Research Institute, La Jolla, CA 92037; <sup>c</sup>School of Artificial Intelligence and Automation, Huazhong University of Science and Technology, Wuhan 430074, China; <sup>d</sup>Department of Biophysics, Sir Run Run Shaw Hospital, Zhejiang University School of Medicine, Hangzhou 310058, China; <sup>e</sup>Department of Pathology, Sir Run Run Shaw Hospital, Zhejiang University School of Medicine, Hangzhou 310058, China; <sup>f</sup>Department of Pharmacology, School of Basic Medical Sciences, Fudan University, Shanghai 200032, China; <sup>g</sup>The CAS Key Laboratory of Receptor Research, Shanghai Institute of Materia Medica, Chinese Academy of Sciences (CAS), Shanghai 201203, China; <sup>h</sup>National Center for Drug Screening, Shanghai Institute of Materia Medica, Chinese Academy of Sciences, Shanghai 201203, China; <sup>i</sup>Research Center for Deep-sea Bioresources, Sanya, Hainan 572025, China; and <sup>j</sup>School of Life Science and Technology, ShanghaiTech University, Shanghai 201210, China

Contributed by Peter K. Vogt, September 2, 2021 (sent for review May 24, 2021; reviewed by John E. Burke and Sandra B. Gabelli)

Phosphoinositide 3-kinases (PI3Ks) are lipid kinases essential for growth and metabolism. Their aberrant activation is associated with many types of cancers. Here we used single-particle cryo-electron microscopy (cryo-EM) to determine three distinct conformations of full-length PI3K $\alpha$  (p110 $\alpha$ -p85 $\alpha$ ): the unliganded heterodimer PI3K $\alpha$ , PI3K $\alpha$  bound to the p110 $\alpha$ -specific inhibitor BYL-719, and PI3K $\alpha$  exposed to an activating phosphopeptide. The cryo-EM structures of unbound and of BYL-719-bound PI3K $\alpha$  are in general accord with published crystal structures. Local deviations are presented and discussed. BYL-719 stabilizes the structure of PI3K $\alpha$ , but three regions of low-resolution extra density remain and are provisionally assigned to the cSH2, BH, and SH3 domains of p85. One of the extra density regions is in contact with the kinase domain blocking access to the catalytic site. This conformational change indicates that the effects of BYL-719 on PI3K $\alpha$  activity extend beyond competition with adenosine triphosphate (ATP). In unliganded PI3K $\alpha$ , the DFG motif occurs in the “in” and “out” positions. In BYL-719-bound PI3K $\alpha$ , only the DFG-in position, corresponding to the active conformation of the kinase, was observed. The phosphopeptide-bound structure of PI3K $\alpha$  is composed of a stable core resolved at 3.8 Å. It contains all p110 $\alpha$  domains except the adaptor-binding domain (ABD). The p85 $\alpha$  domains, linked to the core through the ABD, are no longer resolved, implying that the phosphopeptide activates PI3K $\alpha$  by fully releasing the nSH2 domain from binding to p110 $\alpha$ . The structures presented here show the basal form of the full-length PI3K $\alpha$  dimer and document conformational changes related to the activated and inhibited states.

phosphoinositide 3-kinase (PI3K) | activation | inhibition | activity-dependent conformational changes

PI3Ks (phosphoinositide 3-kinases) are lipid kinases that phosphorylate the 3-hydroxyl group of the inositol ring of phosphatidylinositol (1). They are regulators of numerous important cellular functions, including cell replication, movement, and metabolism (2–6). They are also significant factors in several human diseases, notably in cancer (7).

PI3Ks are grouped into three classes (8). Class I encompasses four isoforms that have shared as well as nonredundant functions (9–11). These are dimeric enzymes consisting of a catalytic subunit, p110, bound to a regulatory subunit. The class is further subdivided into IA and IB. Class IA encompasses the p110 $\alpha$ ,  $\beta$ , and  $\delta$  isoforms. They are predominantly mediating signaling by RTKs (receptor tyrosine kinases). Class IB consists of a single isoform, p110 $\gamma$ , which is activated exclusively by G protein-coupled receptors.

The p110 $\alpha$  isoform and its regulatory subunit p85 $\alpha$  have special importance in cancer (12). Human solid tumors often harbor mutations in p110 $\alpha$ , and about 80% of these mutations are located in three hotspots (13). These are single-nucleotide

substitutions that cause a gain of function in the enzyme (13–17) and are oncogenic in cell culture and in the animal (18–20). p110 $\alpha$  is therefore a promising therapeutic target for cancer.

Numerous PI3K inhibitors have been generated and disclosed (21, 22). Early compounds were “pan-specific,” affecting all four isoforms of class I PI3K. More recently, isoform-specific or isoform-selective inhibitors have been identified. All currently US Food and Drug Administration–approved PI3K inhibitors are either isoform-specific or show distinct preference for one or two isoforms (22). One of the most recently approved compounds is BYL-719 (alpelisib), which is p110 $\alpha$ -specific and is the only PI3K inhibitor currently in clinical use for solid tumors (23–25).

PI3Ks have long been in the crosshairs of structural biologists. The first to be crystallized and analyzed was p110 $\gamma$  and its

## Significance

Phosphoinositide 3-kinases (PI3Ks) are of critical importance in cell signaling and can function as drivers of disease. Information on the PI3K structure is essential for an understanding of the function of these proteins and for the identification of specific and effective small-molecule inhibitors. Here we present a single-particle cryo-electron microscopy (cryo-EM) analysis of PI3K $\alpha$ , the dimer consisting of the p110 $\alpha$  catalytic subunit bound to the p85 $\alpha$  regulatory subunit. We investigated three conformational states of PI3K $\alpha$ : the unbound dimer, the dimer bound to the isoform-specific inhibitor BYL-719, and the dimer associated with an activating phosphopeptide. Each of these conformations reveals specific structural features that provide insights into conformation-associated functions.

Author contributions: S.Y., M.-W.W., and P.K.V. initiated the project; S.Y., J.R.H., M.-W.W., and P.K.V. designed research; S.Y. established the purification protocol for the PI3K $\alpha$  complexes, shared this skill with X.L. and performed bioassays; X.L. and Y.X. performed research, purified the PI3K $\alpha$  complexes, screened specimen and prepared the final samples for negative staining and cryo-EM data collection towards the structures; J.R.H., X.Z., H.Z., Q.Z., T.X., and Y.Z. analyzed data and performed map calculation; J.R.H. conducted structure analysis and built the models; S.Y. and J.R.H. prepared the figures; S.Y., D.Y., M.-W.W., and P.K.V. supervised the studies; and X.L., S.Y., J.R.H., M.-W.W., and P.K.V. wrote the paper with input from all co-authors.

The authors declare no competing interest.

This open access article is distributed under [Creative Commons Attribution-NonCommercial-NoDerivatives License 4.0 \(CC BY-NC-ND\)](https://creativecommons.org/licenses/by-nc-nd/4.0/).

Reviewers: J.E.B., University of Victoria; and S.B.G., Johns Hopkins University.

<sup>1</sup>X.L. and S.Y. are co-first authors.

<sup>2</sup>X.L., S.Y., and J.R.H. contributed equally to this work.

<sup>3</sup>To whom correspondence may be addressed. Email: dhyang@simm.ac.cn, mwwang@simm.ac.cn, or pkvogt@scripps.edu.

This article contains supporting information online at <http://www.pnas.org/lookup/suppl/doi:10.1073/pnas.2109327118/-DCSupplemental>.

Published November 1, 2021.

regulatory subunit (26). This study also defined the functional domains of class I PI3Ks. The crystallographic analysis of the p110 $\alpha$ -p85 $\alpha$  heterodimer was achieved in 2007 (27). By now, more than 40 p110 $\alpha$  structures have been deposited in the Protein Data Bank (PDB; <https://www.rcsb.org/>) (28).

Small-molecule inhibitors have played a significant role in the investigation of the PI3K structure, because they often stabilize the molecule and allow images with higher resolution (21). We took advantage of this stabilizing effect of small molecular ligands by analyzing PI3K $\alpha$  (p110 $\alpha$ -p85 $\alpha$ ) bound to the p110 $\alpha$ -specific inhibitor BYL-719. These investigations address questions of isoform specificity of inhibitors and present data on the position of the DFG domain located in the activation loop of PI3K. They also provide data suggesting that the inhibitory effect of BYL-719 is not confined to competition with adenosine triphosphate (ATP). Our studies further extend to the interaction of PI3K $\alpha$  with an RTK-derived phosphopeptide, representing signal-mediated activation of PI3K.

## Results

**High-Resolution Cryo-EM Structure of PI3K $\alpha$ .** PI3K $\alpha$  was coexpressed in High Five insect cells from a baculovirus dual-expression vector coding for p110 $\alpha$  and p85 $\alpha$ . The PI3K $\alpha$  complex was purified and confirmed by sodium dodecyl sulfate-polyacrylamide gel electrophoresis (SDS-PAGE) for purity (Fig. 1A). Native gel electrophoresis showed that the complex is intact (Fig. 1B). The purified PI3K $\alpha$  exhibits lipid kinase activity as determined by a membrane capture assay (29).

Initial attempts to determine the full-length PI3K $\alpha$  structure were hampered by the aggregation of particles near the edges of holes. These problems were overcome through trial and error of blotting and freezing conditions to obtain particles suitable for analysis. Similar problems have been seen before with the cryo-EM structure of the Regulator complex (30).

The cryo-EM structure of PI3K $\alpha$  was determined by single-particle reconstruction. Vitri-fied complexes were imaged by cryo-EM. After sorting by constitutive two-dimensional (2D) and three-dimensional (3D) classifications, 3D consensus density maps were reconstructed with global resolutions of 2.65 Å for PI3K $\alpha$  (Fig. 1C and D and *SI Appendix, Table S1*) (31). However, local resolution maps showed that different regions of the electron density map have varying resolutions, ranging from 2.0 to 9.3 Å (Fig. 1E). The cryo-EM map allowed us to build an unambiguous model for most regions of the complex, including all domains of p110 $\alpha$  and the nSH2 and iSH2 domains of p85 $\alpha$ , but not the remaining domains of p85 $\alpha$ , which were less well resolved (32). The unmodeled domains are present and observable in the electron density maps (Fig. 1E), but the low resolution of these domains hampers unambiguous assignment (*SI Appendix, Fig. S1*).

The cryo-EM structure of PI3K $\alpha$  shares similar features with structures previously determined with other methods (27, 33) (Fig. 1D). The PI3K $\alpha$  complex exists as an asymmetric heterodimer containing one copy each of p110 $\alpha$  and p85 $\alpha$ . Comparing the cryo-EM structure of PI3K $\alpha$  with the crystal structure of p110 $\alpha$  bound to the truncated p85 $\alpha$  nSH2 (PDB ID code 4OVU) (see *SI Appendix, Table S2* for additional details on PDB ID codes) (33), we found an extensive overall concordance of the two (Fig. 2).

Within the catalytic core of p110 $\alpha$  (residues 109 to 1050), there is only a 1.201-Å rmsd as compared with the reported crystal structure (Fig. 2A). The ABD domain of p110 $\alpha$ , the iSH2 of p85 $\alpha$ , and the nSH2 of p85 $\alpha$  are significantly displaced, leading to a relatively high, 3.425-Å rmsd for these regions. Overall, the cryo-EM structure as compared with the crystal structure has an rmsd of 2.131 Å.

When the cryo-EM and crystal structure data (PDB ID code 4OVU) are aligned using the catalytic core of p110 $\alpha$ , there is a

rotation of the iSH2 domain around residue 538 of p85 $\alpha$ , leading to a displacement of both termini of the iSH2. Additionally, there is a deflection in the loop region of the iSH2 (p85 $\alpha$  residues 498 to 523), resulting in a displacement of S505 C $\alpha$  by 6.9 Å (Fig. 2B). However, when the cryo-EM structure is compared with the crystal structure of the ABD of p110 $\alpha$  and iSH2 of p85 $\alpha$  (PDB ID code 2V1Y) or another structure of PI3K $\alpha$  (PDB ID code 2RD0), these displacements are not present. We suggest that there is some conformational flexibility of the iSH2 and ABD domains with respect to the catalytic core of PI3K, and motion occurs via a flexible hinge at G106.

The structure of nSH2 of p85 $\alpha$  has been investigated many times by both crystallography (34) and NMR (35, 36) and in complex with p110 $\alpha$  (15, 33). Within this domain, the most significant difference between the existing crystal structures and the cryo-EM structure is in the conformation of the BC loop (p110 $\alpha$  residues 361 to 366) (Fig. 2D). Multiple conformations of this loop have been previously observed, both in isolated structures of this domain and in complex with p110 $\alpha$  (34–36). In cryo-EM, we observed the BC loop positioned away from the helical domain and toward the kinase domain.

In addition to the position of this loop, the nSH2 domain is rotated relative to the catalytic core of PI3K. This difference in positioning of the nSH2 has been previously observed (Fig. 2E) (33). The position in the cryo-EM structure more closely aligns with the position seen in the p110 $\alpha$  H1047R mutant structures (15).

In the catalytic domain, the  $\beta$ -sheets forming the N-terminal catalytic lobe (N-lobe) are closer to the active site than observed in the crystal structure (Fig. 2C). This is most pronounced in the  $\beta$ 3K- $\beta$ 4K turn of p110 $\alpha$  residues 774 to 776 with A775 being displaced by 3.1 Å and in the  $\beta$ 4K- $\beta$ 5K turn with I788 displaced by 3.8 Å at the C $\alpha$  positions. These differences might be due to steric interactions with the N-terminal affinity tag present in the crystal structure.

**The Cryo-EM Structure of PI3K $\alpha$  Bound to the p110 $\alpha$ -Specific Inhibitor BYL-719.** In an attempt to stabilize the PI3K $\alpha$  complex, we investigated PI3K inhibitors. The binding of BYL-719 to PI3K $\alpha$  has been previously studied by crystallography (PDB ID code 4JPS) (25). As the resolution of the BYL-719-bound crystal structure was significantly higher than that of the ligand-free complex, we used this compound to stabilize the PI3K $\alpha$  complex for cryo-EM analysis.

BYL-719 is a potent and isoform-specific p110 $\alpha$  inhibitor. As previously reported, BYL-719 almost completely abolishes the lipid kinase activity of PI3K $\alpha$  (Fig. 3A) (37). Using a similar procedure as with the ligand-free complex, 3D consensus density maps were reconstructed with a global resolution of 2.93 Å for BYL-719-bound PI3K $\alpha$  (Fig. 3B and C and *SI Appendix, Table S1*) (38). A molecular model of the BYL-719-bound PI3K $\alpha$  cryo-EM structure was generated, and two orientations are shown in Fig. 3C (39).

Comparison of the cryo-EM structure with the previously reported crystal structure shows many of the same differences that have been identified with the ligand-free structure resulting in an overall rmsd of 2.197 Å (Fig. 3E). Again, the catalytic core of PI3K remains relatively unchanged with an rmsd of 1.690 Å. The iSH2 and ABD domains have a similar rotation as in the ligand-free structure and lead to an rmsd of 3.631 Å. However, there is no rotation of the nSH2, and the BC loop is unobserved in the crystallography data. Similar to the unbound PI3K $\alpha$ , BYL-719-bound PI3K $\alpha$  also shows a displacement of the N-lobe of the kinase domain.

BYL-719 in the cryo-EM structure is in a conformation that is different from the one seen in the crystal structure. However, key interactions designed to confer p110 $\alpha$  specificity are retained (Fig. 3F). Specifically, hydrogen bonds between the



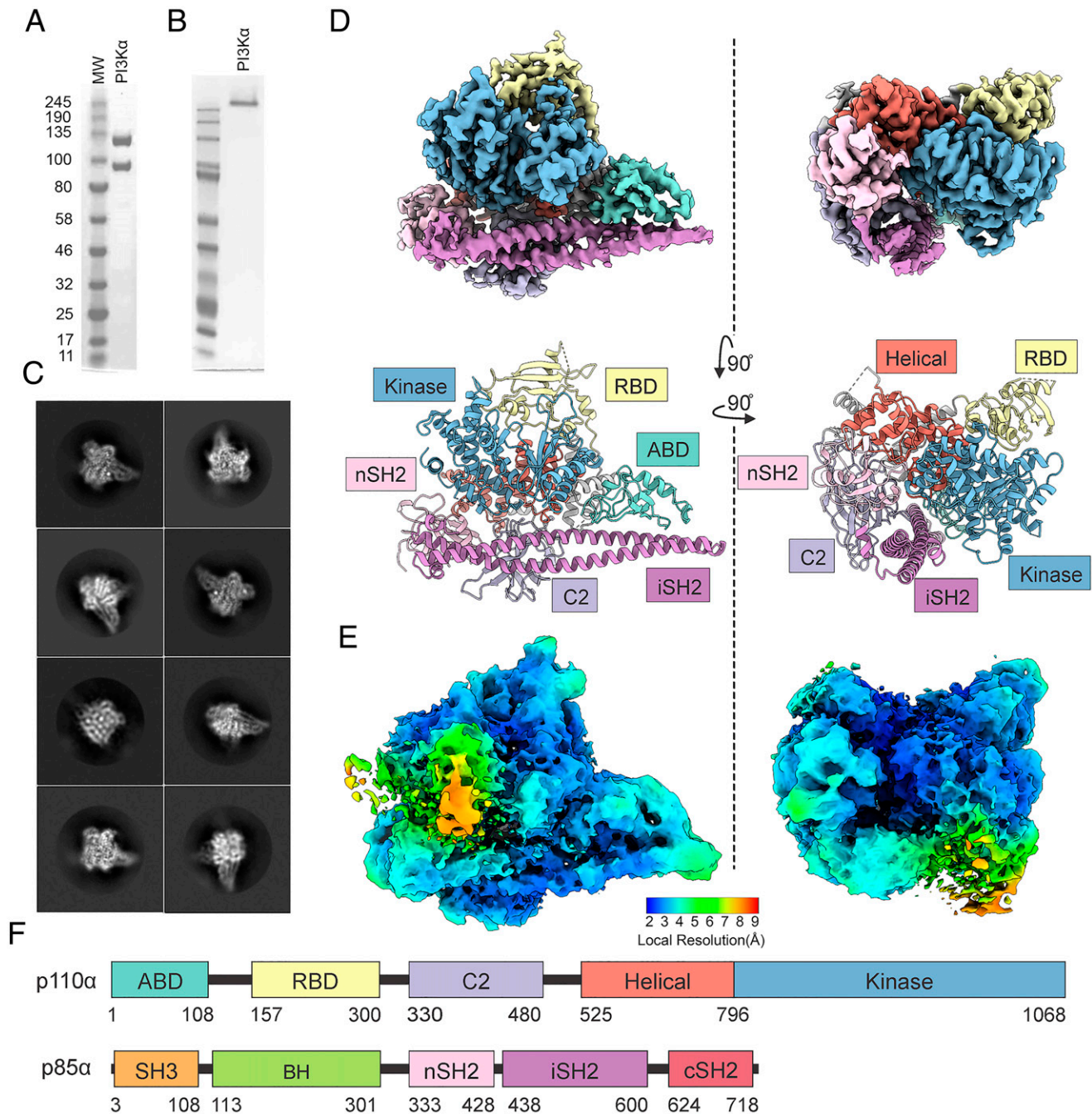


**Fig. 1.** Cryo-EM structure of PI3K $\alpha$ . (A) SDS-PAGE image of the purified PI3K $\alpha$  complex. (B) Native gel image of the purified PI3K $\alpha$  complex. (C) Selected 2D class averages of the PI3K $\alpha$  complex. (D) Cryo-EM density maps and corresponding models of the PI3K $\alpha$  complex in two orientations. (E) Confidence maps of cryo-EM, at 1% FDR, colored by local resolution. (F) Domain structure of p110 $\alpha$  and p85 $\alpha$ .

amide group and Q859 and a hydrogen bond with the carbonyl oxygen of V851 are preserved. However, the position of the CF<sub>3</sub> group is different in the two structures. While the crystal structure has the CF<sub>3</sub> group positioned in a hydrophobic pocket created by P778, I800, K802, and I848, we observed the density of this group rotated by 120°. Instead of a CF–HN hydrogen bond with K802, we observed a CF–HO hydrogen bond with S774. Additionally, the ordered water molecules seen with Y705 and the pyridine nitrogen are not observed by cryo-EM.

**Extra Density.** In the confidence maps for both the unbound PI3K $\alpha$  and BYL-719-bound structures, there are areas of low-

resolution extra density (Figs. 3D and 4A). We have divided the extra density into three regions: ED1, ED2, and ED3, shown in Fig. 4B and *SI Appendix, Fig. S1*. Upon binding of BYL-719, the ED2 region becomes stabilized with local resolution improving from 8 to 5 Å, and the ED3 region can be observed.

There are three domains of p85 left unmodeled in the cryo-EM data: the SH3, BH, and cSH2 domains of p85 $\alpha$ . Using the 1% false discovery rate (FDR) confidence map, we have provisionally assigned ED1, ED2, and ED3 to the cSH2, BH, and SH3 domains, respectively (Fig. 4B). The cSH2 domain of p85 $\beta$  in complex with p110 $\beta$  has been previously solved (40). While the cSH2 domain cannot interact with p110 $\alpha$  in the same

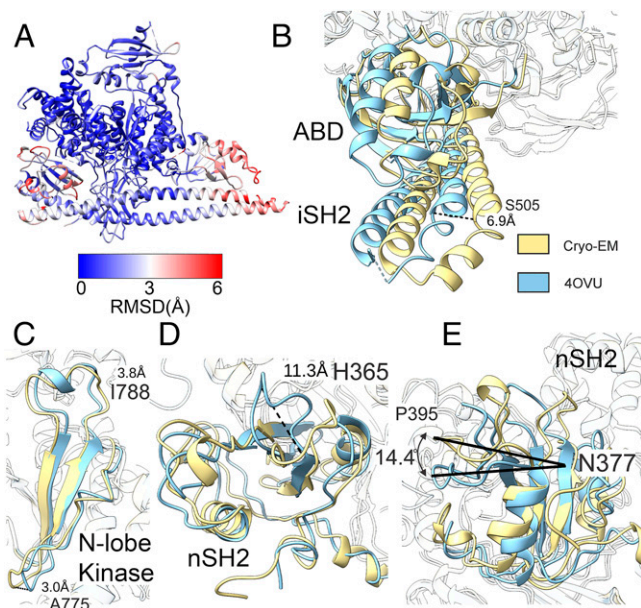


**Fig. 2.** Differences between the cryo-EM structure (gold) and crystal structure (aqua) of PI3K $\alpha$ . (A) Rmsd between cryo-EM and crystal structures (PDB ID code 4OVU) of PI3K $\alpha$ . (B) The ABD and iSH2 domains are displaced by 6.9 Å at the C $\alpha$  of S505. (C) The loops in the N-lobe of the kinase domain are displaced at both A775 and I778. (D) A flexible loop of the nSH2 domain is displaced by 11 Å as measured at the C $\alpha$  of H365. (E) The nSH2 domain is rotated relative to the helical domain by 14°.

manner as with p110 $\beta$ , the volume of ED1 is consistent with the cSH2 domain and the position observed in p110 $\beta$ -p85 $\beta$ . ED2 was assigned to the BH domain based upon its larger size of 180 amino acids and ED3 to the SH3 domain, which is composed of 80 amino acids. However, these domains cannot be unambiguously assigned. Linker regions between the nSH2 and BH domains as well as the iSH2 and cSH2 domains are long enough that either could be ED1 or ED2. Additionally, the linker between the BH and SH3 domains is long enough that it could span the distance from ED1 or ED2 to ED3.

The extra density in the BYL-719-bound structure is in contact with the kinase domain and the iSH2 domain as well as with BYL-719 (Fig. 4C). Specifically, ED2 is in contact with both the N- and C-lobes of the kinase domain, effectively blocking access to the catalytic site (Fig. 4C). Contact with BYL-719 is through the CF<sub>3</sub> group and may be responsible for the positional difference between the cryo-EM and the crystal structures. The contact with the loops of the N-lobe in the BYL-719-bound structure may also explain the rather large rmsd seen for these regions in Fig. 3E.

**Three-Dimensional Variability Analysis.** In both PI3K $\alpha$  structures, there is a large range of local resolutions, particularly around the ED1 to ED3 regions. Three-dimensional variability analysis (3DVA) (41) was performed on both datasets using cryoSPARC.

3DVA demonstrates that ED regions in the unbound PI3K $\alpha$  structure have low local resolution because of large variations in their position and rotation (SI Appendix, Fig. S24). Additionally, there are variations in the iSH2, RBD, nSH2, and kinase domains, which are detailed in SI Appendix, Figs. S2 and S3. The 3DVA of unbound PI3K $\alpha$  includes a component where the DFG motif of the kinase domain rearranges (Fig. 5). In both the unbound PI3K $\alpha$  and BYL-719-bound structures as well as previous structural studies, the DFG motif is in the catalytically active DFG-in conformation (Fig. 5A). However, the 3DVA on the unbound structure (component 3) shows that the DFG

motif can also adopt a DFG-out conformation (Fig. 5B). This conformation has not been seen in 3DVA of the three components analyzed for the BYL-719-bound structure. In the final electron density map of unbound PI3K $\alpha$ , there is indeed a suggestion that the DFG-out conformation could be present in a minority of the particles (Fig. 5A).

**The Cryo-EM Structure of Phosphopeptide-Activated PI3K $\alpha$ .** Activated PI3K was prepared by combining PI3K $\alpha$  with a phosphopeptide derived from PDGFR $\beta$  (platelet-derived growth factor receptor beta) following previously published methods (14). The phosphopeptide increased PI3K $\alpha$  lipid kinase activity (Fig. 6A), as previously reported (42). The cryo-EM analysis of particles of activated PI3K $\alpha$  showed a dramatic departure from the 2D class averages observed for other PI3K $\alpha$  complexes (SI Appendix, Fig. S4), but the particles identified by cryo-EM were not suitable for 3D reconstruction.

However, one 2D class average was obtained with high resolution, and this class is shown alongside similar orientations seen in the PI3K $\alpha$  and BYL-719-bound data (Fig. 6C, with models for comparison in Fig. 6D). The observed 2D class average closely matches the electron density projection of the catalytic core of p110 $\alpha$  without an ABD (PDB ID code 6OAC). Although this orientation is highest in abundance, multiple orientations of the activated complex were observed (SI Appendix, Fig. S4). The data do not indicate a preferred orientation, as the number of particles is well-distributed between different orientations (43, 44). The other orientations are present within the dataset but, because a large proportion of the complex is conformationally flexible with multiple degrees of freedom, these classes have low resolution. In one orientation, the ABD and p85 domains are in a conformation where they do not overlap with the catalytic core, allowing for this particular class to have high resolution. We suggest that this is through the flexibility of the ABD-RBD linker near G106. In theoretical models of possible orientations of the ABD and iSH2 domains, G106 can adopt multiple conformations without clashing or overlapping with the catalytic core while remaining within Ramachandran-allowed regions for glycine. In activated PI3K $\alpha$ , electron density for the nSH2 domain is not observed and electron density for the ABD and iSH2 domains is also absent. Yet native gel electrophoresis (Fig. 6B) shows that the PI3K $\alpha$  complex does not dissociate upon binding to the phosphopeptide. These observations are in accord with the interpretation that when activated, the nSH2, iSH2, and ABD domains no longer interact with the catalytic core of p110 $\alpha$  (residues 107 to 1068). The iSH2 domain remains bound to the ABD domain as demonstrated by native gel electrophoresis, and the ABD domain can adopt a range of conformations upon phosphopeptide binding. The data are compatible with a hypothetical model of phosphopeptide-bound PI3K $\alpha$  in which the catalytic core of p110 $\alpha$ , consisting of the RBD, C2, helical, and kinase domains, forms a rigid group, whereas the ABD and all p85 $\alpha$  domains are flexible, relative to the rigid catalytic core of p110 $\alpha$ .

## Discussion

Our knowledge of the PI3K structure rests on groundbreaking work conducted by X-ray crystallography and hydrogen/deuterium exchange mass spectrometry (HDX-MS) (14, 25, 27, 42, 45). Isolated domains of PI3K have also been investigated by NMR (35, 46, 47). Here we take advantage of recent developments in single-particle analysis in cryo-EM to present structures of PI3K $\alpha$  in different functional conformations. The main technical challenge in the cryo-EM analysis of PI3K $\alpha$  stems from the inherent structural flexibility of several domains, notably the SH3, BH, iSH2, and cSH2 domains of p85 $\alpha$  as well as the ABD domain of p110 $\alpha$ . Despite these obstacles, cryo-EM analysis



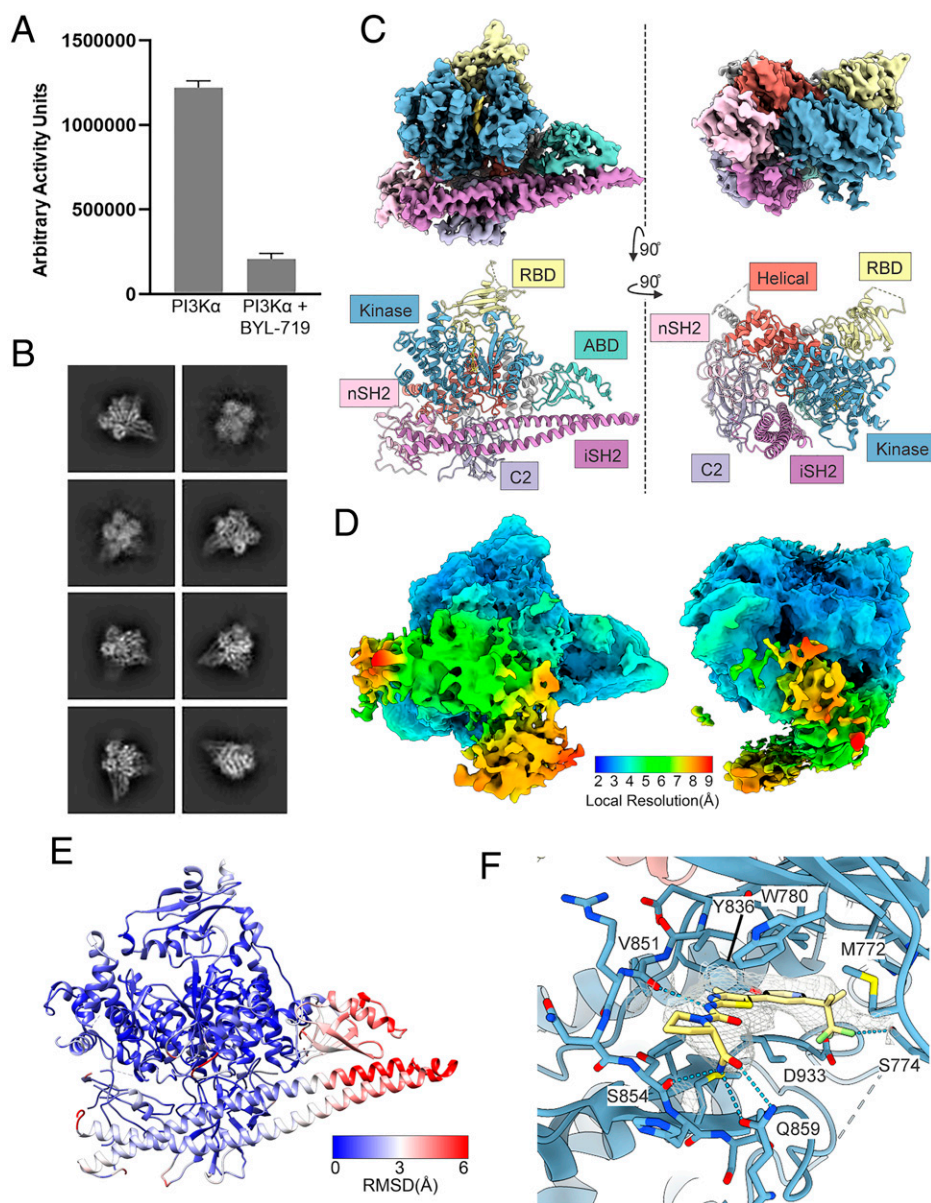


**Fig. 3.** Cryo-EM structure of PI3K $\alpha$  bound to BYL-719. (A) BYL-719 significantly reduces the kinase activity of PI3K $\alpha$  as determined by membrane capture lipid kinase assay. (B) Selected 2D class averages of PI3K $\alpha$  bound to BYL-719. (C) Cryo-EM density maps and corresponding models for PI3K $\alpha$  bound to BYL-719 (gold) shown in two orientations. (D) Confidence maps of cryo-EM, at 1% FDR, colored by local resolution, showing a significant volume of low-resolution electron density. (E) Rmsd between the cryo-EM model and the crystal structure model for BYL-719-bound PI3K $\alpha$  (PDB ID code 4JPS). (F) BYL-719 (yellow) bound to the active site of p110 $\alpha$  forms hydrogen bonds with Q859 and S854 which drive p110 $\alpha$  selectivity. The CF<sub>3</sub> group is in a different orientation and forms a hydrogen bond with S774.

has succeeded in generating data and insights that have not been available by other technologies.

There is extensive concordance between the cryo-EM and crystallography structures. Local deviations have been identified, characterized, and analyzed in detail. One domain that deserves particular attention is the DFG motif. The position of the aspartate of the DFG motif determines the active or inactive state of the kinase. Additionally, small-molecule inhibitors can bind to either the DFG-in or DFG-out conformation (48, 49). Our data show that in unbound PI3K $\alpha$ , DFG is predominantly in the active “in” position, but 3DVA identified a component that shows DFG in the “out” position in a minority of the particles. In the BYL-719-bound structure only the DFG-in conformation, corresponding to the active form of PI3K, has been observed.

The cryo-EM analysis of PI3K $\alpha$  was facilitated by binding to the isoform-specific inhibitor BYL-719. A comparison of the cryo-EM and crystal structures of the bound BYL-719 shows two different conformations, but the interactions that make BYL-719 isoform-specific are preserved and identical in both structures. The use of BYL-719 raises the general issue of the molecular basis of isoform specificity of PI3K inhibitors. This important topic has been reviewed recently (21), emphasizing that isoform specificity is determined by multiple factors that control inhibitor-protein interactions, and that there is no single, universal rule for achieving isoform specificity.

BYL-719 stabilizes areas of extra density, allowing the provisional assignment of the cSH2, BH, and SH3 domains to specific portions of this extra density. In the BYL-719-bound form, SH3, BH, and cSH2 are stably positioned near the

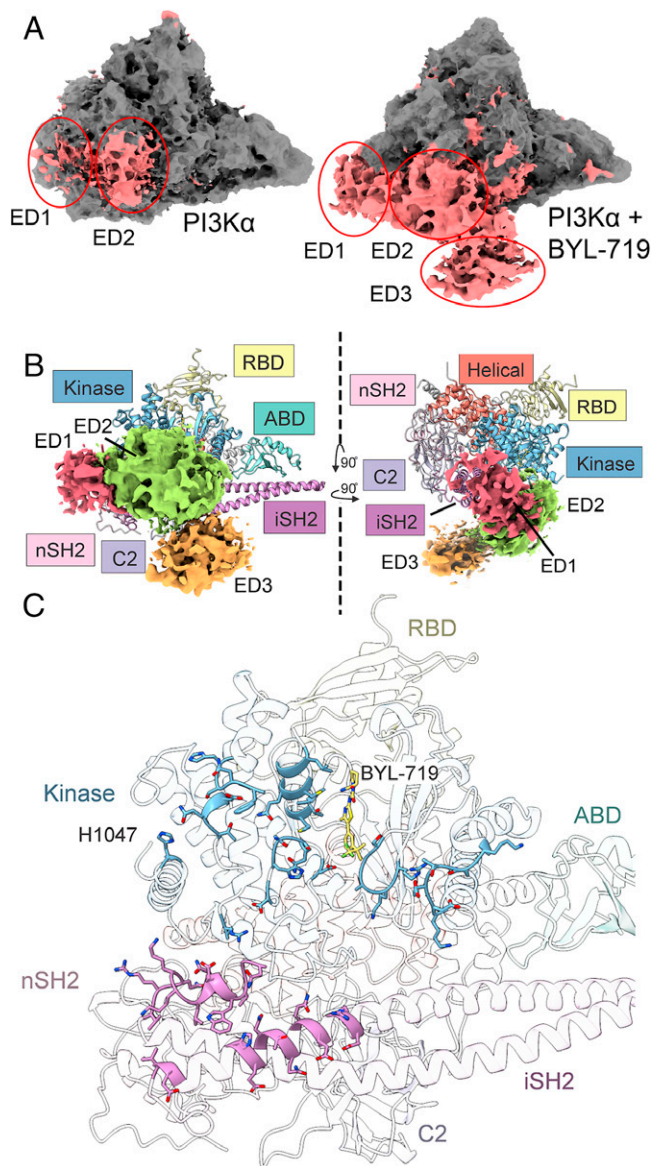


**Fig. 4.** Low-resolution extra density in PI3K $\alpha$  structures. (A) Three regions of extra density are observed in PI3K $\alpha$  and BYL-719-bound structures. (B) The extra density in BYL-719-bound PI3K $\alpha$ . The resolution of these domains is insufficient to model, but the volumes are similar to the unmodeled SH3, BH, and cSH2 domains. We suggest that ED1 is the cSH2 domain (red), ED2 is the BH domain (green), and ED3 (orange) is the SH3 domain. (C) ED2 interacts with several amino acids on the surface of PI3K $\alpha$ , including H1047R, the N- and C-lobes of the kinase domain, and the iSH2 domain. The extra density also interacts directly with BYL-719.

catalytic site. This face of p110 $\alpha$  is known to be involved in binding to the membrane (15, 33) and, by stabilizing the interaction with the p85 $\alpha$  domains on this surface, BYL-719 sterically blocks approach to the membrane and interferes with access of ATP and phosphoinositides. This BYL-719-induced stabilization would cause an inhibition of enzyme activity that is independent of competition with ATP. A small molecule that induces this stable, conformational change could be an effective allosteric inhibitor.

In the unliganded PI3K $\alpha$  the extra density is highly mobile, but we speculate that blocking access to the catalytic site is among the possible positions that could be transiently taken up. This would lead to an attenuation of enzyme activity. A critical

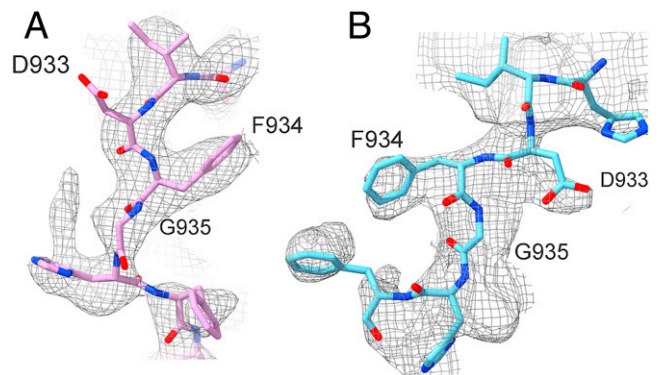


**Fig. 5.** 3DVA of unbound PI3K $\alpha$  contains a DFG-out conformation. (A) The electron density map of the DFG motif of PI3K $\alpha$  shows a DFG-in conformation. (B) 3DVA of PI3K $\alpha$  shows that the DFG motif can also adopt a DFG-out conformation. This conformation is a minor component of the complete dataset.

residue within the catalytic domain is H1047. Many types of cancer carry the gain-of-function mutation H1047R at this site. The mutation leads to the activation of the enzyme through an increased affinity for lipids (15). In contrast to wild-type PI3K $\alpha$  (33), the C terminus of p110 $\alpha$  is flipped in the crystal structure of the H1047R mutant (15, 27). This places the C terminus in a position where it would clash with the ED2 domain. We speculate that the H1047R mutation repositions the ED2 domain, and this may contribute to the activating effect of H1047R. Previous HDX-MS experiments have indeed demonstrated that the H1047R mutation causes increased solvent exchange of the C-lobe of the kinase domain, including residues 848 to 859, 930 to 956, 962 to 980, and 1039 to 1055 (14), which are the regions we suggest are blocked by the ED2 region. Future experiments using the H1047R mutant with full-length p85 $\alpha$  will explore this possibility.

For our studies with activated PI3K $\alpha$ , we offer a hypothetical interpretation that is consonant with the available data. The analysis of these data suggests that all p85 $\alpha$  domains and the ABD of p110 $\alpha$  adopt flexible conformations relative to the p110 $\alpha$  catalytic core. Native gel electrophoresis demonstrated that under these conditions p85 $\alpha$  and p110 $\alpha$  remain bound. Although a 3D reconstruction of the phosphopeptide-activated PI3K $\alpha$  complex could not be achieved, a high-resolution 2D class average of the p110 $\alpha$  catalytic core can be observed and interpreted. Within this class, the nSH2 domain is no longer observed, which is consistent with the proposed mechanism of activation and HDX-MS data of full-length PI3K $\alpha$  (14). Importantly, this projection also lacks the ABD domain and the iSH2 domains (Fig. 6C). This observation indicates that in addition to the nSH2 and cSH2 dissociating from p110 $\alpha$  to bind to an activated RTK, the iSH2 domain dissociates as well. Thus, the catalytic core of p110 $\alpha$  is bound via the ABD-iSH2 interaction to an extended structure containing the nSH2 and cSH2 domains and possibly including the SH3 and BH domains. The connection of the ABD-iSH2 complex to the core functions like a hinge, and we suggest that G106 can act as this hinge. In the long structure extending from the catalytic core, the ABD-iSH2 part is a relatively rigid fiber with flexible globular domains attached to each end by flexible linkers. This long structure could facilitate the conformational flexibility required to reach the phosphorylated tyrosines in the intracellular domain of diverse RTKs (50–52). These tyrosines are located near the membrane but are not necessarily directly adjacent to the membrane. Mobility of the ABD and iSH2 allows for additional conformational flexibility to simultaneously bind RTKs and access phosphatidylinositol (4, 5) bisphosphate (PIP<sub>2</sub>) in the membrane.



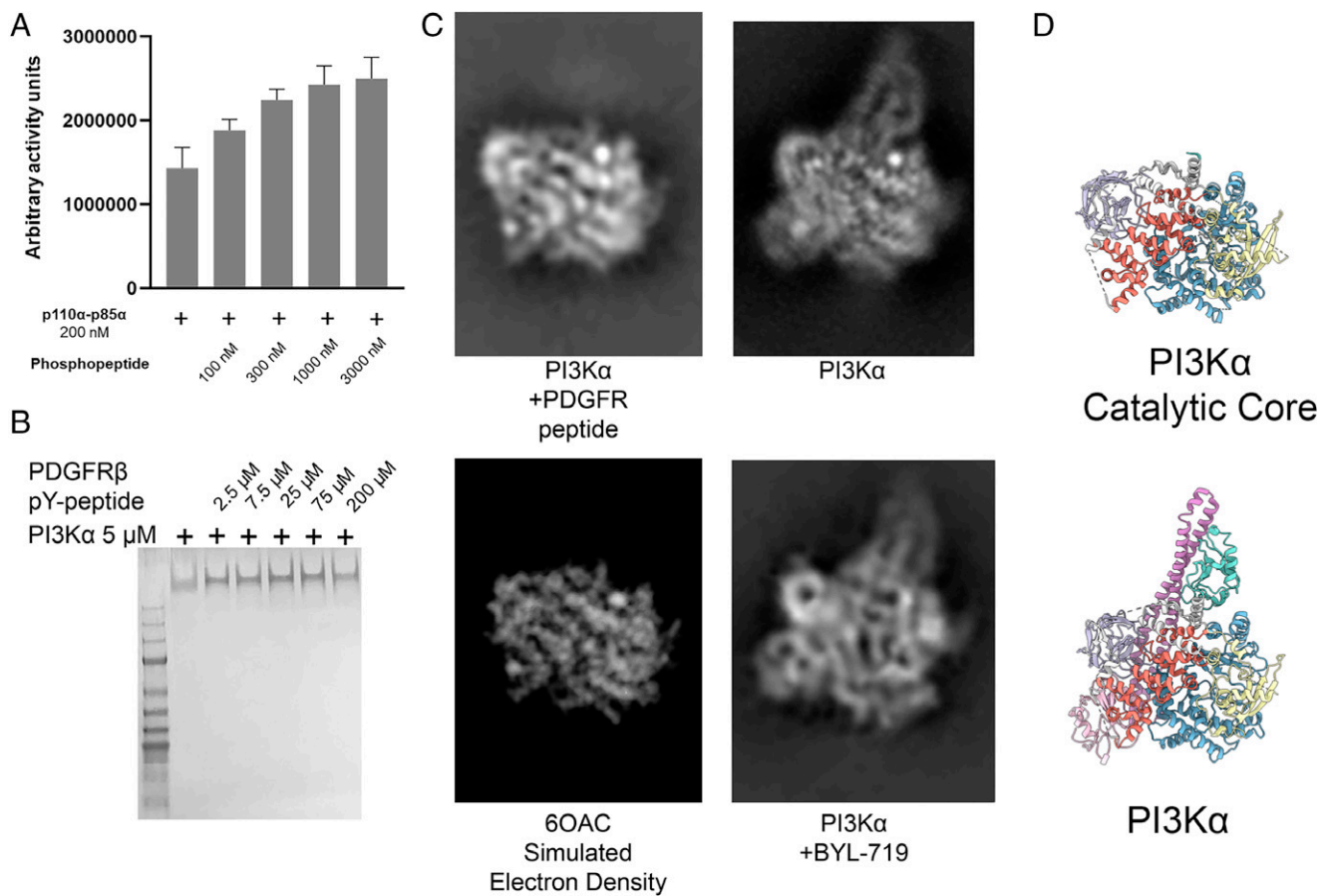


**Fig. 6.** Activation of PI3K $\alpha$  with an activating phosphopeptide as observed by cryo-EM. (A) Quantification of lipid kinase activity from membrane capture assay upon stimulation with a phosphopeptide derived from PDGFR $\beta$ . (B) Native gel electrophoresis of PI3K $\alpha$  with phosphopeptide. p110 $\alpha$  and p85 $\alpha$  dimerization is not disrupted by incubation with the PDGFR $\beta$ -derived phosphopeptide. (C) Comparison of a 2D class average of phosphopeptide-bound PI3K $\alpha$  (Top Left) with an electron density map derived from a crystal structure of p110 $\alpha$  (PDB ID code 6OAC) (Bottom Left) and 2D class averages of unbound and BYL-719-bound PI3K $\alpha$  (Right) in similar orientations for comparison. (D) Models of the catalytic core (Top) and PI3K $\alpha$  (Bottom) in the same orientation as (C) for comparison.

Previously reported structural data for phosphopeptide-activated PI3K $\alpha$  come from HDX-MS experiments (14). In addition to the expected exposure of helical domain amino acids normally bound by the nSH2 domain, activation by the phosphopeptide results in increased solvent exchange of the ABD-RBD linker and C2 domains and, upon lipid binding, the iSH2 domain as well. These observations are consistent with our model of the activated form of PI3K $\alpha$ . The profound structural changes induced in PI3K $\alpha$  by physiological activation raise the question of whether similar changes are mediated by the gain-of-function mutations that show constitutive enzymatic activity, specifically the G106V mutation (53).

Our investigations of the structure of PI3K $\alpha$  suggest some immediate goals for the cryo-EM analysis of PI3K. Other isoforms of class I PI3K would be rewarding targets, and while this manuscript was in revision, the cryo-EM structure of the single member of class IB of PI3K, PI3K $\gamma$  (p110 $\gamma$ -p101), was published (54). The flexibility of PI3K complexes makes the identification of ligands that can stabilize parts or all of the mobile and flexible domains an urgent task. Also on the horizon is the cryo-EM analysis of cancer-specific mutations which would generate further insights into mutant mechanisms of action and could guide the development of mutant-specific inhibitors of therapeutic value. A more generic problem is availability of instrument access. Numerous technical problems still require a time-consuming trial-and-error approach that relies on teamwork and exceptional institutional resources.

However, rapid advances in technology may provide novel solutions.

## Materials and Methods

**Protein Expression and Purification.** A pFastBac dual vector expressing both p110 $\alpha$  and p85 $\alpha$  was kindly provided by Peter Shepherd, University of Auckland, Auckland, New Zealand. The pFastBac dual vector was recombined with the parent bacmid in DH10Bac *Escherichia coli* competent cells to form an expression bacmid containing both p110 $\alpha$  and p85 $\alpha$ . The expression bacmid was then transfected into *Sf9* insect cells for production of recombinant baculovirus. Baculovirus-expressing p110 $\alpha$  with a 6 $\times$  His tag and p85 $\alpha$  were amplified once in *Sf9* insect cells, and then 10 mL amplified baculoviruses were used to infect 1 L BTI-Tn-5B1-4 (High Five) cells at a density of  $1.5 \times 10^6$  cells per milliliter for protein production. Forty-eight hours after infection, High Five cells were harvested by centrifugation at  $1,000 \times g$  for 10 min, washed with ice-cold phosphate-buffered saline, and then pelleted by centrifugation at  $2,000 \times g$  for 10 min. The pellets from 1 L of High Five cell culture were lysed by Dounce homogenization in 60 mL buffer A (20 mM Tris, pH 8.0, 100 mM NaCl, 5% [vol/vol] glycerol, 20 mM imidazole, 0.5% [vol/vol] Triton X-100, and 2 mM  $\beta$ -mercaptoethanol, with ethylenediaminetetraacetate-free protease inhibitor mixture [TargetMol]) on ice, followed by centrifugation for 1 h at  $140,000 \times g$  at 4  $^{\circ}$ C. The supernatant was then passed through a 0.45- $\mu$ m cellulose acetate membrane filter (Merck Millipore) and incubated with Ni-NTA resin (Cytiva) for 2 h at 4  $^{\circ}$ C. The resin was loaded onto a gravity flow column (Sangon Biotech), washed with buffer B (20 mM Tris-HCl, pH 8.0, 400 mM NaCl, 50 mM imidazole, 5% [vol/vol] glycerol, and 2 mM  $\beta$ -mercaptoethanol), and eluted with buffer C (20 mM Tris-HCl, pH 8.0, 100 mM NaCl, 300 mM imidazole, 5% [vol/vol] glycerol, and 2 mM  $\beta$ -mercaptoethanol). The eluate was then loaded onto a 1-mL heparin HP column (Cytiva), washed with buffer D

(20 mM Tris, pH 8.0, 100 mM NaCl, and 2 mM dithiothreitol [DTT]), and eluted with a 0 to 100% gradient of buffer E (20 mM Tris, pH 8.0, 1 M NaCl, and 2 mM DTT). The eluate from the HP column was concentrated to 1 mL using an Amicon 30-kDa centrifugal filter (Millipore) and injected into a Superdex 16/60 200 pg gel filtration column (Cytiva) preequilibrated with buffer F (20 mM Hepes, pH 7.6, 100 mM NaCl, and 5 mM DTT). Fractions of gel filtration were collected, concentrated, aliquoted, and kept at  $-80^{\circ}\text{C}$ .

**Lipid Kinase Assay.** The lipid kinase assays were performed using the membrane capture method as previously published (29). Briefly, purified PI3K $\alpha$  complex was combined with [ $\gamma$ - $^{32}\text{P}$ ]ATP in a kinase buffer with phosphoinositides prepared into vesicles as described (29). Phosphorylated lipids were measured by spotting 4  $\mu\text{L}$  of reaction mixture onto nitrocellulose membrane and washing away unincorporated ATP. The phosphorylated phosphoinositol was measured by autoradiography using a phosphor imager.

#### Cryo-EM Data Acquisition and Image Processing.

**Sample preparation.** The unbound PI3K $\alpha$  was used as is from purification. The purified PI3K $\alpha$  complex (2.5  $\mu\text{L}$ ) at a concentration of 1 mg/mL was spotted onto grids as described below. The BYL-719-bound PI3K $\alpha$  complex was prepared by incubating the PI3K $\alpha$  complex (1 mg/mL) with 1 mM BYL-719 stock (MedChemExpress) at a molar ratio of 1:10 at  $4^{\circ}\text{C}$  for 30 min. The phosphopeptide-bound PI3K $\alpha$  complex was prepared by incubating the PI3K $\alpha$  complex (1 mg/mL) and the phosphopeptide stock (1 mg/mL) at a molar ratio of 1:15 at room temperature for 5 min before vitrification of the sample. Each complex was added to glow-discharged holey carbon grids (Quantifoil R1.2/1.3, 300 mesh) and subsequently vitrified by plunging into liquid ethane using a Vitrobot Mark IV (ThermoFisher Scientific).

**Data acquisition.** Automatic data collection was performed on a Titan Krios equipped with a Gatan K3 Summit direct electron detector. The microscope was operated at 300-kV accelerating voltage, at a nominal magnification of  $46,685\times$  in counting mode, corresponding to a pixel size of 1.045  $\text{\AA}$ . Acquisition parameters are detailed in *SI Appendix, Table S1*.

**Image processing.** Dose-fractionated image stacks were subjected to beam-induced motion correction and dose weighting using MotionCor2.1 (55). A sum of all frames, filtered according to the exposure dose, in each image stack was used for further processing (56). Contrast transfer function parameters for each micrograph were determined by Gctf v1.06 (56). Particle selection and 2D and 3D classifications were performed on a binned dataset with a pixel size of 2.09  $\text{\AA}$  using cryoSPARC (v3.0.1) and RELION-3.0-beta2.

Autopicking yielded particle projections that were subjected to reference-free 2D classification to discard false-positive particles or particles categorized in poorly defined classes, producing projections for further processing. This subset of particle projections was subjected to consecutive rounds of 3D classification with a pixel size of 2.09  $\text{\AA}$  followed by a round of maximum likelihood-based 3D classifications with a pixel size of 2.09  $\text{\AA}$ , resulting in one well-defined subset with projections. Further 3D classifications with a mask on the complex produced one good subset. These were subsequently subjected to another round of 3D classifications with a mask on the complex. A selected subset was then subjected to 3D refinement and Bayesian polishing with a pixel size of 1.045  $\text{\AA}$ . Local resolution was determined using the Bsoft package (v3.0.1) with half-maps as input maps. 3DVA implemented in cryoSPARC was performed to understand and visualize the dynamics in PI3K $\alpha$  complexes.

1. B. Vanhaesebroeck, S. J. Leever, G. Panayotou, M. D. Waterfield, Phosphoinositide 3-kinases: A conserved family of signal transducers. *Trends Biochem. Sci.* **22**, 267–272 (1997).
2. L. E. Rameh, L. C. Cantley, The role of phosphoinositide 3-kinase lipid products in cell function. *J. Biol. Chem.* **274**, 8347–8350 (1999).
3. R. Katso *et al.*, Cellular function of phosphoinositide 3-kinases: Implications for development, homeostasis, and cancer. *Annu. Rev. Cell Dev. Biol.* **17**, 615–675 (2001).
4. M. J. Fry, Structure, regulation and function of phosphoinositide 3-kinases. *Biochim. Biophys. Acta* **1226**, 237–268 (1994).
5. E. Castellano *et al.*, RAS signalling through PI3-kinase controls cell migration via modulation of Reelin expression. *Nat. Commun.* **7**, 11245 (2016).
6. J. S. Yu, W. Cui, Proliferation, survival and metabolism: The role of PI3K/AKT/mTOR signalling in pluripotency and cell fate determination. *Development* **143**, 3050–3060 (2016).
7. D. A. Fruman *et al.*, The PI3K pathway in human disease. *Cell* **170**, 605–635 (2017).
8. S. Jean, A. A. Kiger, Classes of phosphoinositide 3-kinases at a glance. *J. Cell Sci.* **127**, 923–928 (2014).
9. B. Bilanges, Y. Posor, B. Vanhaesebroeck, PI3K isoforms in cell signalling and vesicle trafficking. *Nat. Rev. Mol. Cell Biol.* **20**, 515–534 (2019).
10. B. Vanhaesebroeck, M. A. Whitehead, R. Piñeiro, Molecules in medicine mini-review: Isoforms of PI3K in biology and disease. *J. Mol. Med. (Berl.)* **94**, 5–11 (2016).
11. B. Vanhaesebroeck, J. Guillemet-Guibert, M. Graupera, B. Bilanges, The emerging mechanisms of isoform-specific PI3K signalling. *Nat. Rev. Mol. Cell Biol.* **11**, 329–341 (2010).

**Low-Resolution Maps.** Low-resolution maps were produced from the unsharpened cryo-EM map by applying a B-factor blur of 100  $\text{\AA}^2$  using REFMAC5 (v5.8.0267) (57). Additional maps used the 1% FDR confidence maps generated from half-maps by CCP-EM (v1.5.0.0-ge0b9395d) (58).

**Preparation of Electron Density Projection of PDB ID Code 6OAC.** PDB ID code 6OAC (59) was converted to an electron density volume map using pdb2mrc (v2.12) (60). Using Chimera (61), the structure was visualized as a solid projection to produce the image in Fig. 6C.

**Model Building.** The X-ray crystal structure of PI3K $\alpha$  with BYL-719 (PDB ID code 4JPS) (25) was docked into the cryo-EM map using phenix.dock\_in\_map (v1.19-2-4158) (62). Models were constructed using X-ray crystal structure information from PDB ID code 2IUG (34) for portions of the nSH2 domain, PDB ID code 2V1Y (45) for portions of the iSH2, and PDB ID code 6VO7 (63) for portions of the RBD domain. Geometric restraints for BYL-719 were created using phenix.eLBOW (64). Maps were density-modified using phenix.resolve (65). Coordinates were refined in real space using phenix.real\_space\_refine (66); maps were sharpened using phenix.autosharpen (67) and Coot (0.9.2-pre EL) (68). Model validation was performed using phenix.validation\_cryoem (69), which uses MolProbity (70). The model of PI3K $\alpha$  was produced by docking the structure containing BYL-719 into the cryo-EM map and refined using a similar procedure as for the BYL-719-containing structure.

**Figures.** Figures were produced using Chimera (v1.14 build 42094) (61) and ChimeraX (v1.2 2021-05-24) (71). Protein alignments between models were produced using Chimera MatchMaker (72) using the catalytic core of p110 $\alpha$  (residues 108 to 1047) instead of PI3K $\alpha$ .

**Data Availability.** The electron density maps and atomic coordinates for unbound PI3K $\alpha$  and the BYL-719-bound PI3K $\alpha$  complex reported in this article have been deposited in the Electron Microscopy Data Bank (EMDB) with ID codes EMD-24081 (31) and EMD-24082 (38) and in the Protein Data Bank with ID codes 7MYN (32) and 7MYO (39), respectively. All other study data are included in the article and/or *SI Appendix*.

**ACKNOWLEDGMENTS.** We thank M. Lei, P. F. Lan, and H. Sun for technical assistance, and H. E. Xu and S. B. Li for valuable discussions. This work was supported by National Natural Science Foundation of China 81872915 (to M.-W.W.), 82073904 (to M.-W.W.), 81922071 (to Y.Z.), 81773792 (to D.Y.), 81973373 (to D.Y.), and 21704064 (to Q.Z.); National Science & Technology Major Project of China–Key New Drug Creation and Manufacturing Program 2018ZX09735–001 (to M.-W.W.) and 2018ZX09711002–002–005 (to D.Y.); National Key Basic Research Program of China 2018YFA0507000 (to M.-W.W.) and 2019YFA0508800 (to Y.Z.); Novo Nordisk-CAS Research Fund Grant NNCAS-2017–1-CC (to D.Y.); National Cancer Institute Awards R35 CA197582 (to P.K.V.) and R50 CA243899 (to J.R.H.). The content is solely the responsibility of the authors and does not necessarily represent the official views of the NIH. The cryo-EM data were collected at the Cryo-Electron Microscopy Research Center, Shanghai Institute of Materia Medica, Chinese Academy of Sciences. We also wish to express our gratitude to Anja Zembrzycki, who expertly handled all aspects of the manuscript from early drafts to submission and revision.

12. M. Martini, M. C. De Santis, L. Braccini, F. Gulluni, E. Hirsch, PI3K/AKT signaling pathway and cancer: An updated review. *Ann. Med.* **46**, 372–383 (2014).
13. Y. Samuels *et al.*, High frequency of mutations of the PIK3CA gene in human cancers. *Science* **304**, 554 (2004).
14. J. E. Burke, O. Perisic, G. R. Masson, O. Vadas, R. L. Williams, Oncogenic mutations mimic and enhance dynamic events in the natural activation of phosphoinositide 3-kinase p110 $\alpha$  (PIK3CA). *Proc. Natl. Acad. Sci. U.S.A.* **109**, 15259–15264 (2012).
15. D. Mandelker *et al.*, A frequent kinase domain mutation that changes the interaction between PI3K $\alpha$  and the membrane. *Proc. Natl. Acad. Sci. U.S.A.* **106**, 16996–17001 (2009).
16. S. J. Isakoff *et al.*, Breast cancer-associated PIK3CA mutations are oncogenic in mammary epithelial cells. *Cancer Res.* **65**, 10992–11000 (2005).
17. T. Ikenoue *et al.*, Functional analysis of PIK3CA gene mutations in human colorectal cancer. *Cancer Res.* **65**, 4562–4567 (2005).
18. A. G. Bader, S. Kang, P. K. Vogt, Cancer-specific mutations in PIK3CA are oncogenic in vivo. *Proc. Natl. Acad. Sci. U.S.A.* **103**, 1475–1479 (2006).
19. Y. Samuels *et al.*, Mutant PIK3CA promotes cell growth and invasion of human cancer cells. *Cancer Cell* **7**, 561–573 (2005).
20. S. Kang, A. G. Bader, P. K. Vogt, Phosphatidylinositol 3-kinase mutations identified in human cancer are oncogenic. *Proc. Natl. Acad. Sci. U.S.A.* **102**, 802–807 (2005).
21. M. S. Miller, P. E. Thompson, S. B. Gabelli, Structural determinants of isoform selectivity in PI3K inhibitors. *Biomolecules* **9**, 82 (2019).



22. A. E. Garces, M. J. Stocks, Class 1 PI3K clinical candidates and recent inhibitor design strategies: A medicinal chemistry perspective. *J. Med. Chem.* **62**, 4815–4850 (2019).
23. H. S. Rugo *et al.*, Time course and management of key adverse events during the randomized phase III SOLAR-1 study of PI3K inhibitor alpelisib plus fulvestrant in patients with HR-positive advanced breast cancer. *Ann. Oncol.* **31**, 1001–1010 (2020).
24. F. André *et al.*; SOLAR-1 Study Group, Alpelisib for *PIK3CA*-mutated, hormone receptor-positive advanced breast cancer. *N. Engl. J. Med.* **380**, 1929–1940 (2019).
25. P. Furet *et al.*, Discovery of NVP-BYL719 a potent and selective phosphatidylinositol-3 kinase alpha inhibitor selected for clinical evaluation. *Bioorg. Med. Chem. Lett.* **23**, 3741–3748 (2013).
26. E. H. Walker, O. Perisic, C. Ried, L. Stephens, R. L. Williams, Structural insights into phosphoinositide 3-kinase catalysis and signalling. *Nature* **402**, 313–320 (1999).
27. C. H. Huang *et al.*, The structure of a human p110alpha/p85alpha complex elucidates the effects of oncogenic PI3Kalpha mutations. *Science* **318**, 1744–1748 (2007).
28. H. M. Berman *et al.*, The Protein Data Bank. *Nucleic Acids Res.* **28**, 235–242 (2000).
29. Z. A. Knight, M. E. Feldman, A. Balla, T. Balla, K. M. Shokat, A membrane capture assay for lipid kinase activity. *Nat. Protoc.* **2**, 2459–2466 (2007).
30. K. B. Rogala *et al.*, Structural basis for the docking of mTORC1 on the lysosomal surface. *Science* **366**, 468–475 (2019).
31. X. Liu *et al.*, Cryo-EM Structure of p110alpha in complex with p85alpha. Electron Microscopy Data Bank. <https://www.emdataresource.org/EMD-24081>. Deposited 20 May 2021.
32. X. Liu *et al.*, Cryo-EM Structure of p110alpha in complex with p85alpha. Protein Data Bank. <https://www.rcsb.org/structure/7MYN>. Deposited 20 May 2021.
33. M. S. Miller *et al.*, Structural basis of nSH2 regulation and lipid binding in PI3K $\alpha$ . *Oncotarget* **5**, 5198–5208 (2014).
34. R. T. Nolte, M. J. Eck, J. Schlessinger, S. E. Shoelson, S. C. Harrison, Crystal structure of the PI 3-kinase p85 amino-terminal SH2 domain and its phosphopeptide complexes. *Nat. Struct. Biol.* **3**, 364–374 (1996).
35. G. W. Booker *et al.*, Structure of an SH2 domain of the p85 alpha subunit of phosphatidylinositol-3-OH kinase. *Nature* **358**, 684–687 (1992).
36. T. Weber, B. Schaffhausen, Y. Liu, U. L. Günther, NMR structure of the N-SH2 of the p85 subunit of phosphoinositide 3-kinase complexed to a doubly phosphorylated peptide reveals a second phosphotyrosine binding site. *Biochemistry* **39**, 15860–15869 (2000).
37. C. Fritsch *et al.*, Characterization of the novel and specific PI3K $\alpha$  inhibitor NVP-BYL719 and development of the patient stratification strategy for clinical trials. *Mol. Cancer Ther.* **13**, 1117–1129 (2014).
38. X. Liu *et al.*, Cryo-EM structure of p110alpha in complex with p85alpha inhibited by BYL-719. Electron Microscopy Data Bank. <https://www.emdataresource.org/EMD-24082>. Deposited 20 May 2021.
39. X. Liu *et al.*, Cryo-EM structure of p110alpha in complex with p85alpha inhibited by BYL-719. Protein Data Bank. <https://www.rcsb.org/structure/7MYO>. Deposited 20 May 2021.
40. X. Zhang *et al.*, Structure of lipid kinase p110 $\beta$ /p85 $\beta$  elucidates an unusual SH2-domain-mediated inhibitory mechanism. *Mol. Cell* **41**, 567–578 (2011).
41. A. Punjani, D. J. Fleet, 3D variability analysis: Resolving continuous flexibility and discrete heterogeneity from single particle cryo-EM. *J. Struct. Biol.* **213**, 107702 (2021).
42. J. E. Burke, R. L. Williams, Dynamic steps in receptor tyrosine kinase mediated activation of class IA phosphoinositide 3-kinases (PI3K) captured by H/D exchange (HDX-MS). *Adv. Biol. Regul.* **53**, 97–110 (2013).
43. B. Li, D. Zhu, H. Shi, X. Zhang, Effect of charge on protein preferred orientation at the air-water interface in cryo-electron microscopy. *J. Struct. Biol.* **213**, 107783 (2021).
44. A. J. Noble *et al.*, Reducing effects of particle adsorption to the air-water interface in cryo-EM. *Nat. Methods* **15**, 793–795 (2018).
45. N. Miled *et al.*, Mechanism of two classes of cancer mutations in the phosphoinositide 3-kinase catalytic subunit. *Science* **317**, 239–242 (2007).
46. G. W. Booker *et al.*, Solution structure and ligand-binding site of the SH3 domain of the p85 alpha subunit of phosphatidylinositol 3-kinase. *Cell* **73**, 813–822 (1993).
47. G. Siegal *et al.*, Solution structure of the C-terminal SH2 domain of the p85 alpha regulatory subunit of phosphoinositide 3-kinase. *J. Mol. Biol.* **276**, 461–478 (1998).
48. H. Möbitz, The ABC of protein kinase conformations. *Biochim. Biophys. Acta* **1854**, 1555–1566 (2015).
49. Z. Zhao *et al.*, Exploration of type II binding mode: A privileged approach for kinase inhibitor focused drug discovery? *ACS Chem. Biol.* **9**, 1230–1241 (2014).
50. J. F. Flynn, C. Wong, J. M. Wu, Anti-EGFR therapy: Mechanism and advances in clinical efficacy in breast cancer. *J. Oncol.* **2009**, 526963 (2009).
51. I. Garajová, E. Giovannetti, G. Biasco, G. J. Peters, c-Met as a target for personalized therapy. *Transl. Oncogenomics* **7** (suppl. 1), 13–31 (2015).
52. J. M. Kavan *et al.*, How IGF-1 activates its receptor. *eLife* **3**, e03772 (2014).
53. M. L. Rudd *et al.*, A unique spectrum of somatic PIK3CA (p110alpha) mutations within primary endometrial carcinomas. *Clin. Cancer Res.* **17**, 1331–1340 (2011).
54. M. K. Rathinaswamy *et al.*, Structure of the phosphoinositide 3-kinase (PI3K) p110 $\gamma$ -p101 complex reveals molecular mechanism of GPCR activation. *Sci. Adv.* **7**, eabj4282 (2021).
55. S. Q. Zheng *et al.*, MotionCor2: Anisotropic correction of beam-induced motion for improved cryo-electron microscopy. *Nat. Methods* **14**, 331–332 (2017).
56. K. Zhang, Gctf: Real-time CTF determination and correction. *J. Struct. Biol.* **193**, 1–12 (2016).
57. G. N. Murshudov *et al.*, REFMAC5 for the refinement of macromolecular crystal structures. *Acta Crystallogr. D Biol. Crystallogr.* **67**, 355–367 (2011).
58. M. Beckers, A. J. Jakobi, C. Sachse, Thresholding of cryo-EM density maps by false discovery rate control. *IUCr* **6**, 18–33 (2019).
59. D. Rageot *et al.*, (S)-4-(difluoromethyl)-5-(4-(3-methylmorpholino)-6-morpholino-1,3,5-triazin-2-yl)pyridin-2-amine (PQR530), a potent, orally bioavailable, and brain-penetrable dual inhibitor of class I PI3K and mTOR kinase. *J. Med. Chem.* **62**, 6241–6261 (2019).
60. G. Tang *et al.*, EMAN2: An extensible image processing suite for electron microscopy. *J. Struct. Biol.* **157**, 38–46 (2007).
61. E. F. Pettersen *et al.*, UCSF Chimera—A visualization system for exploratory research and analysis. *J. Comput. Chem.* **25**, 1605–1612 (2004).
62. D. Liebschner *et al.*, Macromolecular structure determination using X-rays, neutrons and electrons: Recent developments in Phenix. *Acta Crystallogr. D Struct. Biol.* **75**, 861–877 (2019).
63. N. G. Martinez *et al.*, Biophysical and structural characterization of novel RAS-binding domains (RBDs) of PI3K $\alpha$  and PI3K $\gamma$ . *J. Mol. Biol.* **433**, 166838 (2021).
64. N. W. Moriarty, R. W. Grosse-Kunstleve, P. D. Adams, electronic Ligand Builder and Optimization Workbench (eLBOW): A tool for ligand coordinate and restraint generation. *Acta Crystallogr. D Biol. Crystallogr.* **65**, 1074–1080 (2009).
65. T. C. Terwilliger, S. J. Ludtke, R. J. Read, P. D. Adams, P. V. Afonine, Improvement of cryo-EM maps by density modification. *Nat. Methods* **17**, 923–927 (2020).
66. P. D. Adams *et al.*, PHENIX: A comprehensive Python-based system for macromolecular structure solution. *Acta Crystallogr. D Biol. Crystallogr.* **66**, 213–221 (2010).
67. T. C. Terwilliger, O. V. Sobolev, P. V. Afonine, P. D. Adams, Automated map sharpening by maximization of detail and connectivity. *Acta Crystallogr. D Struct. Biol.* **74**, 545–559 (2018).
68. P. Emsley, B. Lohkamp, W. G. Scott, K. Cowtan, Features and development of Coot. *Acta Crystallogr. D Biol. Crystallogr.* **66**, 486–501 (2010).
69. P. V. Afonine *et al.*, New tools for the analysis and validation of cryo-EM maps and atomic models. *Acta Crystallogr. D Struct. Biol.* **74**, 814–840 (2018).
70. C. J. Williams *et al.*, MolProbity: More and better reference data for improved all-atom structure validation. *Protein Sci.* **27**, 293–315 (2018).
71. T. D. Goddard *et al.*, UCSF ChimeraX: Meeting modern challenges in visualization and analysis. *Protein Sci.* **27**, 14–25 (2018).
72. E. C. Meng, E. F. Pettersen, G. S. Couch, C. C. Huang, T. E. Ferrin, Tools for integrated sequence-structure analysis with UCSF Chimera. *BMC Bioinformatics* **7**, 339 (2006).